Research Article | Vol. 29, No. 14 / 5 July 2021 / Optics Express 21348
Optics EXPRESS

Extreme polarization-dependent supercontinuum generation in an uncladded silicon nitride waveguide

EIRINI TAGKOUDI,[1] CAROLINE G. AMIOT,[2] GOËRY GENTY,[2] AND CAMILLE-SOPHIE BRÈS[1,*]

[1] *École Polytechnique Fédérale de Lausanne, Photonic Systems Library (PHOSL), CH-1015, Switzerland*
[2] *Tampere University, Photonics Laboratory, Ultrafast Photonics Group, FI-33014 Tampere, Finland*
[*] *camille.bres@epfl.ch*

Abstract: We experimentally demonstrate the generation of a short-wave infrared supercontinuum in an uncladded silicon nitride (Si_3N_4) waveguide with extreme polarization sensitivity at the pumping wavelength of 2.1 µm. The air-clad waveguide is specifically designed to yield anomalous dispersion regime for transverse electric (TE) mode excitation and all-normal-dispersion (ANDi) at near-infrared wavelengths for the transverse magnetic (TM) mode. Dispersion engineering of the polarization modes allows for switching via simple adjustment of the input polarization state from an octave-spanning soliton fission-driven supercontinuum with fine spectral structure to a flat and smooth ANDi supercontinuum dominated by a self-phase modulation mechanism (SPM). Such a polarization sensitive supercontinuum source offers versatile applications such as broadband on-chip sensing to pulse compression and few-cycle pulse generation. Our experimental results are in very good agreement with numerical simulations.

1. Introduction

Supercontinuum generation (SCG) in nonlinear fibers and waveguides has been extensively studied over the past 20 years and a wide range of pump source-waveguide configurations has been reported [1–8]. More recently, emphasis has shifted towards the development of on-chip supercontinuum (SC) sources with very broad spectral coverage [9] yet with a considerably reduced footprint. Such integrated solutions are ideal from practical applications perspective, with significant potential for spectroscopy, frequency metrology and sensing [10].

On-chip SCG in integrated waveguides has been demonstrated using various materials including aluminum nitride (AlN) [11,12], chalcogenide glass [13,14], indium gallium phosphide (InGaP) [15], lithium niobate ($LiNbO_3$) [16–18], and tantalum pentoxide (Ta_2O_5) [19]. While particularly impressive results have been obtained with some of these materials, SCG in integrated complementary metal-oxide-semiconductor (CMOS) platforms with mature fabrication processes possibly offers better prospects for all-integrated solutions. And indeed, silicon-based approaches such as silicon-on-insulator (SOI) [20,21], Si-on-sapphire [22], silicon nitride [10,23–25], or silicon germanium (SiGe) [26–30] have attracted significant interest for SCG. Among those, stoichiometric silicon nitride (Si_3N_4) waveguides, with transparency extending from the visible up to the mid-infrared and able of sustaining high power, represent an attractive solution for SCG [30]. The mature fabrication technology combined with design flexibility enable a large dispersion landscape while keeping propagation losses at a low level. An additional benefit arising from the dispersion properties and transparency window of these waveguides is their compatibility with standard telecommunication grade sources or novel turn-key thulium doped fiber sources that can be used to seed the supercontinuum generation process [31,32].

Supercontinuum dynamics dramatically depend on the dispersion characteristics and nearly all previous studies of on-chip SCG in Si_3N_4 waveguides use standard telecommunication wavelength

#430197 https://doi.org/10.1364/OE.430197
Journal © 2021 Received 28 Apr 2021; revised 10 Jun 2021; accepted 10 Jun 2021; published 22 Jun 2021

Optics EXPRESS

femtosecond pumps in the anomalous dispersion region [10,23,25]. Recently, the generation of SC in a Si_3N_4 waveguide using a 2 μm fiber laser has also been reported in the anomalous dispersion regime [31]. In this regime, the spectral broadening arises from soliton dynamics including fission of the seed pulse into multiple fundamental solitons and energy transfer to phase-matched dispersive waves (DW) [33]. While these dynamics are known to yield SC with a very large spectral bandwidth, they are also very sensitive to noise and lead to spectra with fine spectral structures [33]. The noise-sensitivity and fine spectral features can be significantly reduced in platforms with all-normal dispersion (ANDi). ANDi SCG typically exhibits reduced bandwidth compared to anomalous pumping schemes, but because the generating dynamics are essentially dominated by self-phase modulation (SPM) which is much less susceptible to noise amplification, the obtained SC generally possesses improved phase-stability and coherence [34,35] which makes it ideal for pulse compression applications [33,36,37]. While ANDi SCG has attracted significant attention in fiber-based platforms [37,38], there have been very few demonstrations of on-chip ANDi SC, mostly in silicon germanium waveguides exploiting the strong normal material dispersion [27,28]. However, accessing this regime required the use of bulky optical parametric amplifier pumps. On the other hand, ANDi SCG in silicon-rich nitride platform with low normal GVD for the TE mode has been recently reported [39] using telecom wavelength pumping. While the bandwidth of the generated SC spanned nearly one octave, the spectrum showed once again spectral features with intensity variations across the SC spectrum in excess of 30 dB.

In this work, for the first time to our knowledge, we demonstrate short-wave infrared SCG with extreme polarization-sensitive dynamics in an uncladded Si_3N_4 waveguide platform using a 2.1 μm pump laser. Dispersion-engineering of the air-clad waveguide geometry yields all-normal-dispersion (ANDi) at near-infrared wavelengths for the transverse magnetic (TM) mode and anomalous dispersion for transverse electric (TE) mode excitation. One can exploit this dramatic change in the dispersion profile to switch from a smooth and highly coherent ANDi SC spectrum with 700 nm of bandwidth to an octave-spanning soliton fission-driven SC with a spectral coverage from the visible up to 3.0 μm, by rotating the polarization of the input pulses. Numerical simulations are in a very good agreement with the experiments. Our results open up new perspectives for the generation of versatile broadband light sources whose characteristics can be tailored to diverse applications by simply tuning the input polarization of the seed pulses. For example, with the design demonstrated here, the output can be varied from a stable and smooth spectrum for pulse compression and few-cycle pulse generation to an octave-spanning SC with fine structures for direct on-chip sensing and spectroscopic applications.

2. Experimental setup and waveguide

The waveguide is fabricated using the photonic Damascene process [40] based on low-pressure chemical vapor deposition (LPCVD) of Si_3N_4 on top of silicon dioxide (SiO_2). This technique exploits the substrate topography to release efficiently the tensile stress and prevents cracking of the Si_3N_4 thin film, allowing for the fabrication of large cross-section waveguides. The Si_3N_4 core layer is left uncovered, providing a full air-cladded scheme that can be used for sensing applications. The waveguide has a cross-section of 2 μm × 0.75 μm with calculated numerical aperture (NA) of 0.5 and 0.7 for the TE and TM mode, respectively. A scanning electron microscope (SEM) picture of the fabricated structure and corresponding dimensions are shown in the inset of Fig. 1(a). The waveguide is 5.5 cm long, folded in 11 meanders on a 5mm x 5mm chip. The meanders have a bend radius of approximately 175 μm, designed to reduce mode mixing between the fundamental modes and their higher-order counterparts. Simulations of the waveguide properties using a finite element method mode solver (COMSOL Multiphysics, see Data File 1) show high mode confinement for the fundamental mode up to 3 μm. The uncladded waveguide further includes short tapered sections on both input and output

Optics EXPRESS

sides to ensure optimum coupling to the fundamental mode [41]. While in principle one cannot completely rule out that a small fraction of the injected light leaks out to higher-order modes, we nevertheless believe that the SC is generated in the fundamental mode, as also confirmed by the very good agreement between the experimental results and numerical simulations assuming only single-mode propagation.

The group velocity dispersion (GVD) profile numerically simulated for both TM and TE modes is shown in Fig. 1(a). We can see that, for the TE mode, the dispersion is essentially low and anomalous in the 1-2 μm region with two zero-dispersion wavelengths (ZDWs) at 1 and 2.2 μm. The dispersion of the TM mode is also anomalous in the near-infrared with ZDWs at 850 nm and 1.78 μm but it becomes strongly normal for wavelengths above 2 μm.

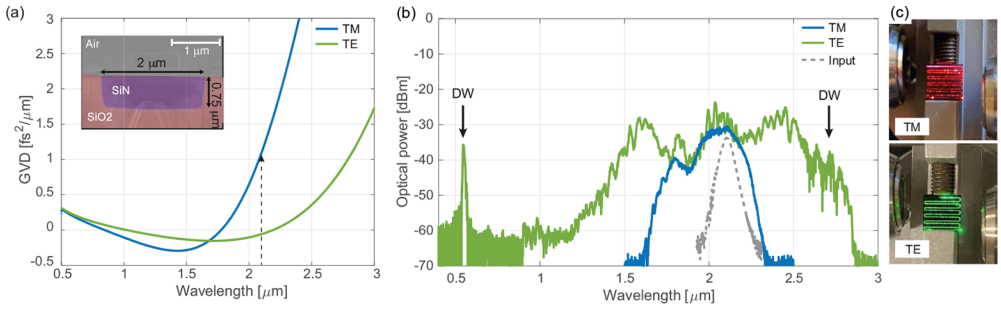

Fig. 1. (a) Simulated group velocity dispersion (GVD) for the fundamental TE (green) and for fundamental TM mode (blue). The dotted arrow indicates the position of the pump. Inset: SEM image of the Si_3N_4 waveguide. (b) Experimental spectra measured at the output of the 5.5 cm long waveguide for TE (green) and TM (blue) mode coupling. The incident peak power is estimated to be 48 kW and 54 kW for the TE and TM mode, respectively. The spectrum of the attenuated pump pulse is also shown (gray). The theoretically predicted DW locations are indicated by the arrows. (c) Photographs of the waveguide taken from the top showing red scattered light for TM excitation, and green scattered light for TE excitation.

A turn-key thulium-doped fiber mode-locked laser (NOVAE Brevity λ+) producing 78 fs (FWHM) pulses at 2.1 μm with 19 MHz repetition rate is used as the pump source. Light is injected and coupled out of the waveguide using a set of identical aspheric chalcogenide lenses. The coupled power is adjusted using a variable optical attenuator and the polarization of the pump pulses is controlled by a half wave-plate, allowing to excite selectively the TE or TM mode. As a result of the coupling optics, the pulses injected into the waveguide are slightly chirped and their duration increased to 110 fs. At the waveguide output, the collimated light is focused with a parabolic mirror into a fluoride multimode fiber (MMF) connected to an optical spectrum analyzer (OSA). Depending on the wavelength range, the spectra are recorded using different OSAs for the visible/near-infrared range from 350 nm to 1750 nm (Yokogawa AQ6374) and the mid-infrared range 1500-3400 nm (Yokogawa AQ6376). The total transmission losses including in/out-coupling, propagation losses, and Fresnel reflection from the waveguide facets were measured at the pump wavelength and at low power in the absence of spectral broadening. They are estimated to be around 13 and 22 dB for TE and TM polarization, respectively.

3. Results and analysis

Fig. 1(b) shows the experimentally recorded spectra at the output of the waveguide for an incident average power of 100 mW and 112 mW for TE and TM input polarization, respectively. These values correspond to 48 kW and 54 kW peak powers incident on the coupling optics. Estimating the actual fraction of peak power effectively injected into the waveguide is not straightforward. This is because it is difficult to distinguish the coupling losses from the propagation losses for a

Optics EXPRESS

multi-curve waveguide geometry, as the one used here. In all experiments reported below, we therefore refer to the incident peak power which is the parameter that can be reliably measured.

One can see a striking difference between the SC spectra generated in the two modes, caused by the different generating mechanisms. Specifically, in the TE mode, the anomalous waveguide dispersion at the pump wavelength enables soliton-fission driven SCG whereby the input pulse breaks up into fundamental solitons and energy is simultaneously transferred to phase-matched DWs located in the normal dispersion region. In order to support this interpretation, we calculated the theoretical DW wavelengths from [33]:

$$\beta(\omega) - \beta(\omega_s) - \frac{1}{v_g}(\omega - \omega_s) = \frac{\gamma P_0}{2}, \tag{1}$$

where β is the propagation constant, ω_s, v_g, and P_0 are the central frequency, group-velocity, and peak power of the input pulse, and γ is the nonlinear coefficient. Expanding the propagation constant into a Taylor series and neglecting the nonlinear contribution, one can rewrite the phase-matching condition as:

$$\sum_{m\geq 2} \frac{(\omega - \omega_s)^m}{m!}\beta_m \cong 0. \tag{2}$$

where β_m represents the m^{th} order dispersion coefficient. The predicted DW wavelengths at λ_{DW1} $\approx$ 547 nm and $\lambda_{DW2} \approx$ 2.70 µm indicated by the arrows in Fig. 1(b) are in excellent agreement with the measured spectrum. The result is an octave-spanning SC spectrum extending from the visible to the mid-infrared. The fact that the pump wavelength is located much closer to the second zero-dispersion wavelength leads to the generation of an infrared DW close to the pump wavelength and a DW in the visible isolated from the SC spectrum. Changing the input polarization for TM pumping leads to a limited but smooth and flat SC spectrum typical of the ANDi regime and essentially dominated by SPM. Photographs of the chip taken with a standard camera are shown in Fig. 1(c) for both TE and TM pumping, further highlight the two different regimes observed depending on the input polarization. In the case of TM pumping, one can see the generation and scattering of red light near 700 nm from the input of the waveguide arising from third-harmonic generation (THG) of the pump. In the case of TE pumping, we did not observe THG. Instead, we clearly see the generation of green light corresponding to the DW generated at 547 nm. In contrast with THG, the DW is not generated instantly from the waveguide input but after a distance of few mm, corresponding to the point of maximum higher-order soliton temporal compression and fission. In order to confirm our initial observations, we carried out a more detailed experimental and numerical study of the SC generation mechanism in both polarization modes.

3.1. Soliton fission-driven supercontinuum

We begin by illustrating in Fig. 2(a) the experimental evolution of the spectrum in the TE-anomalous regime for increasing peak power. At an incident peak power of 1.3 kW, we start observing the generation of a DW component in the mid-infrared at around 2.7 µm. Increasing the pump power to about 12 kW, the spectrum experiences significant broadening and we observe a DW generated in the visible. Further increase of the incident power leads to additional expansion, in particular towards the short wavelengths and increased amplitude of the visible DW component.

In order to understand better the physical mechanisms behind the spectral broadening, we performed numerical simulations of the pulse propagation dynamics using the generalized nonlinear Schrödinger equation (GNLSE). The GNLSE is solved with a second-order Runge–Kutta algorithm in the frame of reference moving at the group-velocity of the input pulse and including high-order dispersion terms up to the 10^{th} order. The dispersion profiles correspond to those shown in Fig. 1(a), calculated using COMSOL Multiphysics. The model also includes the

Optics EXPRESS

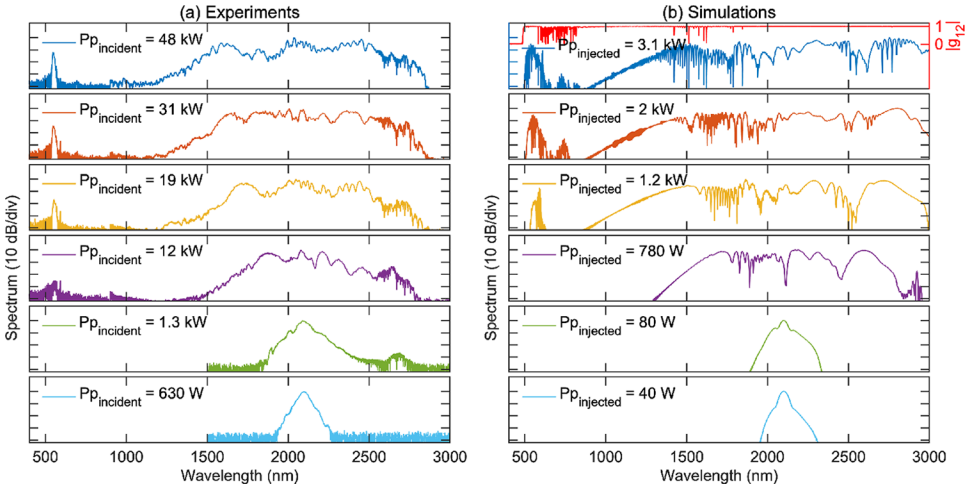

Fig. 2. (a) Experimental SCG for TE excitation for increasing incident peak power. (b) Simulated SCG for injected peak power values as indicated. The simulated first-order degree of coherence for the highest peak power value at the output of the waveguide is plotted in red.

wavelength-dependence of the nonlinear coefficient and modes effective area. The nonlinear refractive index is assumed to be $n_2 = 2.4\times10^{-19}$ m^{2}W^{-1} [42]. The Raman response is negligible for Si_3N_4 waveguides and it is therefore not included. The temporal intensity of the pump pulses is assumed to be hyperbolic secant (sech^2) with input chirp as in our experiments. The injected peak power was scaled proportionally from the experimentally measured peak power incident on the coupling optics by a fixed coupling coefficient used as a free-running parameter. With this approach, we found the fraction of incident peak power coupled into the TE and TM mode that matches best with our experimental observations to be 8% and 15%, respectively.

The simulated SC spectrum for TE input polarization is shown in Fig. 2(b) as a function of injected peak power. In particular, the spectral shape, bandwidth, and location of the DWs are well predicted by the simulations. We do note some discrepancy in the long wavelengths side at the largest power value where the simulated spectra extends further compared to the experiments. This discrepancy may be attributed to the uncertainty on the simulated dispersion profile which assumes a constant cross-section without any imperfections. Indeed, in the strong confinement regime in which the waveguide operates, small deviations at the sub-micron scale of the cross-section dimensions affect the dispersion profile such that the ideal simulated profile may partially differ from that of the actual waveguide. Additional losses in the long wavelengths induced by the waveguide bends could also explain the discrepancy observed.

To confirm the nature of the soliton dynamics that leads to the SC generation in the TE mode, Fig. 3 plots the simulated SC spectral and temporal evolution corresponding to the highest incident peak power value in our experiments. The spectral evolution shows an initial phase of near-symmetric broadening with maximum expansion observed after about 4 mm. In the time domain, the pulse corresponds to higher-order soliton experiencing self-focusing dynamics with maximum temporal compression reached after 4 mm. This distance is slightly larger than what seen in the experiments above (approximately 3 mm), and we attribute this difference to deviation from the ideal dispersion profile used in the numerical simulations. At this point in the propagation, the spectrum expands significantly into the normal dispersion regime and higher-order dispersion leads to fission of the compressed pulse into two fundamental solitons. The fission is further accompanied by the generation of two distinct DWs in the normal dispersion regions at 550 nm and 2.7 μm, respectively, which rapidly walk off from the pump

Optics EXPRESS

temporal residue. Because the DWs in the infrared and visible experience reduced and increased group-delay as compared to the pump residue, they respectively appear at the leading and trailing edge of the temporal window. The ejected solitons during the fission process experience a strong spectral recoil towards the short wavelengths from the strong DW component at 2.7 μm, inducing a downshift of their central wavelength and resulting in the solitons to be located at the negative times in the temporal window. We also note that, once ejected and in the absence of Raman gain, the fundamental solitons exhibit a quasi-linear trajectory in the space-time plane. Propagation beyond the fission distance leads to some interactions between the solitons and DWs yielding a small increase in the SC spectral bandwidth but the spectral broadening process is essentially complete after 1 cm. These dynamics are confirmed from the simulated spectrogram at the output of the waveguide, shown in Fig. 4, where we can clearly identify the solitons ejected from the fission process and DWs generated in the visible and in the mid-infrared by the soliton with largest amplitude (spectrogram animation is presented in Visualization 1). We also verified the noise-sensitivity of the generated SC spectrum and used for this purpose stochastic numerical simulations of the GNLSE using a one photon per mode spectral noise background with random phase [33]. The calculated complex degree of first-order coherence $g_{12}^{(1)}$ given by:

$$g_{12}^{(1)}(\lambda) = \frac{\langle E_1^*(\lambda) E_2(\lambda) \rangle}{\sqrt{\langle |E_1(\lambda)|^2 \rangle \langle |E_2(\lambda)|^2 \rangle}}, \tag{3}$$

where E_1^* and E_2 are conjugate pairs of individual supercontinuum complex spectral envelopes calculated for 100 independent realizations with different noise seeds is shown in red in Fig. 2(b) for the highest injected peak power value. One can see that the spectrum essentially overall maintains a high level of coherence over the entire SC bandwidth, although we do observe small fluctuations around the wavelength of the solitons and visible DW (Fig. 2(b) top sub-panel).

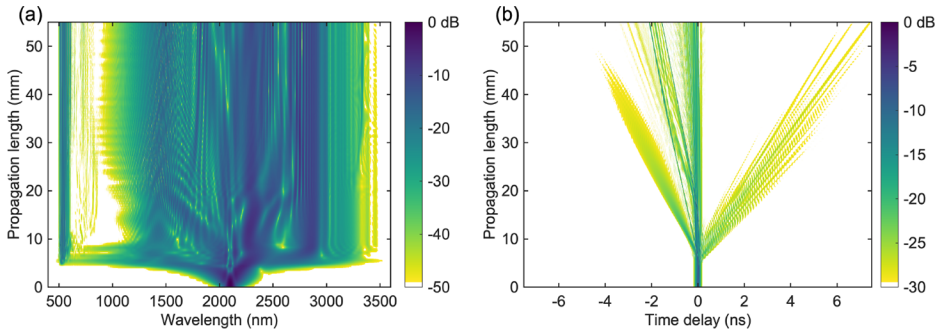

Fig. 3. Simulated (a) spectral and (b) temporal normalized evolution when pulses with 3.1 kW peak power are injected in the TE mode.

3.2. *ANDi supercontinuum*

The experimental evolution of the spectrum as a function of pump power for TM mode excitation is shown in Fig. 5(a). At lower power values, we observe symmetrical spectral broadening due to SPM. For increased pump power, the spectrum exhibits asymmetry with enhanced broadening towards the shorter wavelengths due to the strong group-velocity dispersion slope and reduced dispersion below 2 μm (see Fig. 1(a)). Numerical simulations confirm this behaviour (Fig. 5(b)) and are found to be in good agreement with the experimental results. The simulated spectral and temporal evolution in the TM mode plotted in Fig. 6 for the maximum coupled power shows typical ANDi SCG dynamics. One can see that SCG occurs mainly in the first few mm of the waveguide. The SPM-dominated spectral broadening is initially symmetrical and as the spectrum

Optics EXPRESS

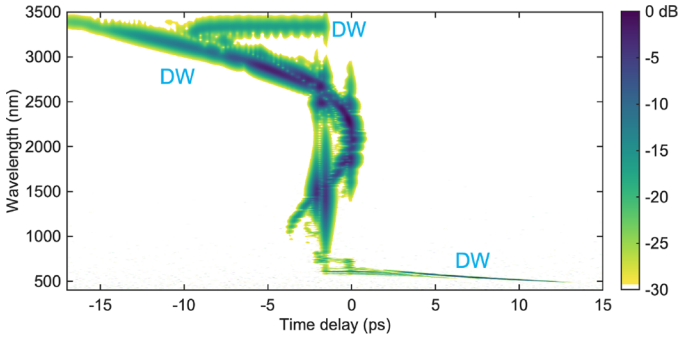

Fig. 4. Simulated spectrogram of supercontinuum in TE mode at the output of the waveguide for a maximum coupled peak power of 3.1 kW. DW: dispersive waves.

expands the asymmetry becomes more pronounced due to higher-order dispersion. In the time domain, the input pulse gradually stretches due to the large normal dispersion which prevents additional nonlinear spectral broadening beyond 5 mm. Significantly, the supercontinuum is highly coherent as shown by the solid red line (Fig. 5(b) top sub-panel) and the associated temporal envelope is a single pulse with limited fine structure.

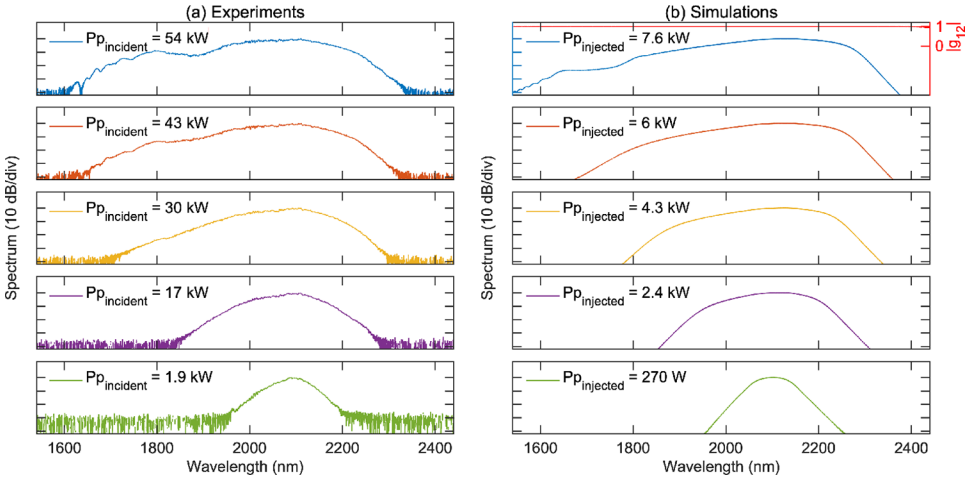

Fig. 5. (a) Experimental SCG for TM-ANDi SCG for increasing incident peak power. (b) Simulated SCG for injected peak power as indicated. The simulated first-order degree of coherence for the highest peak power at the output of the waveguide is plotted in red.

Due to the strong normal dispersion regime in TM excitation, one may expect the SC pulses to exhibit quasi-linear chirp. In order to confirm this, we show in Fig. 7(a) the simulated spectrogram of the ANDi supercontinuum at the waveguide output for the maximum input peak power. The spectrogram shows a single pulse that has been stretched to approximately 6 ps at the waveguide output (see the animated spectrogram in Visualization 2). The corresponding spectral phase shown in 7(b) is very smooth and quasi-parabolic across the entire spectral envelope such that the temporal SC pulse could be compressible. Using a dispersion grating with 1 nm spectral resolution and spatial light modulator with 1024 pixels to compensate for the spectral phase over 1600-2300 nm range, the compressed pulse would be about 27 fs (see Fig. 7(c)), corresponding to about 4 optical cycles with a small residual pedestal. Of course, it is important to bear in mind that the numerical results above assume an ideal input pulse profile and that deviations from a

Optics EXPRESS

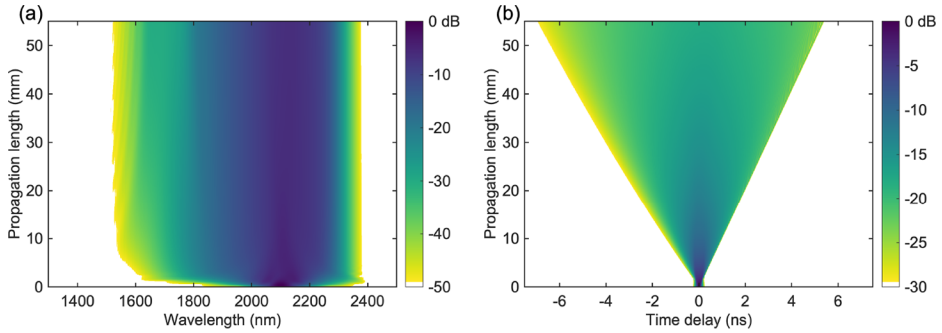

Fig. 6. Simulated (a) spectral and (b) temporal normalized evolution when pulses with 7.6 kW peak power are injected in the TM mode.

noiseless pump pulse may lead to imperfections in ANDi SCG and limit post-compression [43]. Nevertheless, the phase-stability in ANDi SC generation is still significantly better as compared to the anomalous dispersion pumping scheme and we believe that on-chip ANDi SC generation could be promising avenue for few-cycle pulse generation, particularly in the mid-infrared.

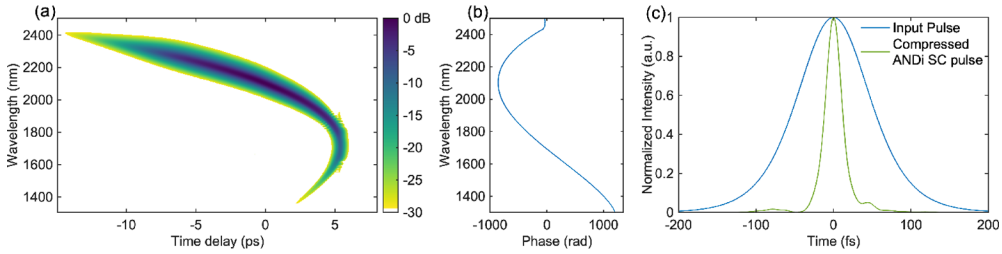

Fig. 7. (a) Simulated spectrogram of ANDi supercontinuum in TM mode at the output of the waveguide for a maximum coupled peak power of 7.6 kW. (b) Spectral phase of the SC at the output of the waveguide. (c) Simulated normalized temporal intensity profile of the ANDi pulse after post-compression using a dispersion grating and spatial light modulator (green solid line). For comparison the temporal intensity profile of the input pulse is also shown (blue solid line).

4. Conclusion

We have demonstrated short-wave infrared supercontinuum generation in an uncladded Si_3N_4 waveguide with extreme polarization sensitivity. Leveraging TM/TE dispersion engineering of the waveguide, one can obtain SC spectra at the waveguide output with very different characteristics by simply adjusting the input polarization. Specifically, with TM excitation one seeds the generation of a flat, SPM-dominated all-normal dispersion SC spanning from 1.75 µm to 2.35 µm with high power density and high degree of coherence. TE injection yields an octave-spanning SC extending up to 3 µm, essentially driven by soliton dynamics. Our experimental measurements are in good agreement with numerical simulations. Having both anomalous and ANDi SCG from a single waveguide offers significant flexibility. One can simultaneously benefit from both regimes in a simple design and favor either SC regime depending on the intended application, e.g. for on-chip spectroscopy and sensing with the TE mode, or pulse compression and few-cycle pulse generation with the TM mode.

Funding. Schweizerischer Nationalfonds zur Förderung der Wissenschaftlichen Forschung (182414 (LEAD));

Optics EXPRESS

European Research Council (CoG PISSARRO (ERC-2017-CoG 771647)); Academy of Finland (298463, 318082, Flagship PREIN 320165).

Acknowledgments. Authors would like to acknowledge Junqiu Liu from K-lab of EPFL for the fabrication of the uncladded Si_3N_4 waveguide.

Disclosures. The authors declare no conflicts of interest.

Data availability. Data underlying the results presented in this paper are not publicly available at this time but may be obtained from the authors upon reasonable request.

References

1. J. Chiles, N. Nader, E. J. Stanton, D. Herman, G. Moody, J. Zhu, J. C. Skehan, B. Guha, A. Kowligy, J. T. Gopinath, K. Srinivasan, S. A. Diddams, I. Coddington, N. R. Newbury, J. M. Shainline, S. W. Nam, and R. P. Mirin, "Multifunctional integrated photonics in the mid-infrared with suspended AlGaAs on silicon," Optica **6**(9), 1246–1254 (2019).
2. C. Lafforgue, S. Guerber, J. M. Ramirez, G. Marcaud, C. Alonso-Ramos, X. L. Roux, D. Marris-Morini, E. Cassan, C. Baudot, F. Boeuf, S. Cremer, S. Monfray, and L. Vivien, "Broadband supercontinuum generation in nitrogen-rich silicon nitride waveguides using a 300 mm industrial platform," Photon. Res. **8**(3), 352–358 (2020).
3. K. Hammani, L. Markey, M. Lamy, B. Kibler, J. Arocas, J. Fatome, A. Dereux, J.-C. Weeber, and C. Finot, "Octave spanning supercontinuum in titanium dioxide waveguides," Appl. Sci. **8**(4), 543–554 (2018).
4. T. S. Saini, N. P. T. Hoa, K. Nagasaka, X. Luo, T. H. Tuan, T. Suzuki, and Y. Ohishi, "Coherent midinfrared supercontinuum generation using a rib waveguide pumped with 200 fs laser pulses at 2.8 μm," Appl. Opt. **57**(7), 1689–1693 (2018).
5. J. R. Woods, J. Daykin, A. S. Tong, C. Lacava, P. Petropoulos, A. C. Tropper, P. Horak, J. S. Wilkinson, and V. Apostolopoulos, "Supercontinuum generation in tantalum pentoxide waveguides for pump wavelengths in the 900 nm to 1500 nm spectral region," Opt. Express **28**(21), 32173–32184 (2020).
6. N. Singh, D. Vermulen, A. Ruocco, N. Li, E. Ippen, F. X. Kärtner, and M. R. Watts, "Supercontinuum generation in varying dispersion and birefringent silicon waveguide," Opt. Express **27**(22), 31698–31712 (2019).
7. S. May, M. Clerici, and M. Sorel, "Supercontinuum generation in dispersion engineered AlGaAs-on-insulator waveguides," Sci. Rep. **11**(1), 2052 (2021).
8. D. R. Carlson, D. D. Hickstein, A. Lind, J. B. Olson, R. W. Fox, R. C. Brown, A. D. Ludlow, Q. Li, D. Westly, H. Leopardi, T. M. Fortier, K. Srinivasan, S. A. Diddams, and S. B. Papp, "Photonic-chip supercontinuum with tailored spectra for counting optical frequencies," Phys. Rev. Applied **8**(1), 014027 (2017).
9. D. Y. Oh, K. Y. Yang, C. Fredrick, G. Ycas, S. A. Diddams, and K. J. Vahala, "Coherent ultra-violet to near-infrared generation in silica ridge waveguides," Nat. Commun. **8**, 1–7 (2017)..
10. R. Halir, Y. Okawachi, J. Levy, M. Foster, M. Lipson, and A. Gaeta, "Ultrabroadband supercontinuum generation in a cmos-compatible platform," Opt. Lett. **37**(10), 1685–1687 (2012).
11. D. D. Hickstein, H. Jung, D. R. Carlson, A. Lind, I. Coddington, K. Srinivasan, G. G. Ycas, D. C. Cole, A. Kowligy, C. Fredrick, S. Droste, E. S. Lamb, N. R. Newbury, H. X. Tang, S. A. Diddams, and S. B. Papp, "Ultrabroadband supercontinuum generation and frequency-comb stabilization using on-chip waveguides with both cubic and quadratic nonlinearities," Phys. Rev. Applied **8**(1), 014025 (2017).
12. J. Lu, X. Liu, A. W. Bruch, L. Zhang, J. Wang, J. Yan, and H. X. Tang, "Ultraviolet to mid-infrared supercontinuum generation in single-crystalline aluminum nitride waveguides," Opt. Lett. **45**(16), 4499–4502 (2020).
13. Y. Yu, X. Gai, P. Ma, D.-Y. Choi, Z. Yang, R. Wang, S. Debbarma, S. J. Madden, and B. Luther-Davies, "A broadband, quasi-continuous, mid-infrared supercontinuum generated in a chalcogenide glass waveguide," Laser & Photonics Reviews **8**(5), 792–798 (2014).
14. B. Kuyken, M. Billet, F. Leo, K. Yvind, and M. Pu, "Octave-spanning coherent supercontinuum generation in an AlGaAs-on-insulator waveguide," Opt. Lett. **45**(3), 603–606 (2020).
15. U. D. Dave, C. Ciret, S.-P. Gorza, S. Combrie, A. De Rossi, F. Raineri, G. Roelkens, and B. Kuyken, "Dispersive-wave-based octave-spanning supercontinuum generation in InGaP membrane waveguides on a silicon substrate," Opt. Lett. **40**(15), 3584–3587 (2015).
16. C. Phillips, C. Langrock, J. Pelc, M. Fejer, J. Jiang, M. E. Fermann, and I. Hartl, "Supercontinuum generation in quasi-phase-matched $LiNbO_3$ waveguide pumped by a Tm-doped fiber laser system," Opt. Lett. **36**(19), 3912–3914 (2011).
17. J. Lu, J. B. Surya, X. Liu, Y. Xu, and H. X. Tang, "Octave-spanning supercontinuum generation in nanoscale lithium niobate waveguides," Opt. Lett. **44**(6), 1492–1495 (2019).
18. M. Yu, B. Desiatov, Y. Okawachi, A. L. Gaeta, and M. Lončar, "Coherent two-octave-spanning supercontinuum generation in lithium-niobate waveguides," Opt. Lett. **44**(5), 1222–1225 (2019).
19. R. Fan, C.-L. Wu, Y.-Y. Lin, C.-Y. Liu, P.-S. Hwang, C.-W. Liu, J. Qiao, M.-H. Shih, Y.-J. Hung, Y.-J. Chiu, A.-K. Chu, and C.-K. Lee, "Visible to near-infrared octave spanning supercontinuum generation in tantalum pentoxide (Ta_2O_5) air-cladding waveguide," Opt. Lett. **44**(6), 1512–1515 (2019).
20. N. Singh, M. Xin, D. Vermeulen, K. Shtyrkova, N. Li, P. T. Callahan, E. S. Magden, A. Ruocco, N. Fahrenkopf, C. Baiocco, B. P.-P. Kuo, S. Radic, E. Ippen, F. X. Kärtner, and M. R. Watts, "Octave-spanning coherent supercontinuum generation in silicon on insulator from 1.06 μm to beyond 2.4 μm," Light Sci Appl **7**(1), 17131 (2018).

Optics EXPRESS

21. H. Saghaei and V. Van, "Broadband mid-infrared supercontinuum generation in dispersion-engineered silicon-on-insulator waveguide," JOSA B **36**(2), A193–A202 (2019).
22. N. Singh, D. D. Hudson, and B. J. Eggleton, "Silicon-on-sapphire pillar waveguides for mid-ir supercontinuum generation," Opt. Express **23**(13), 17345–17354 (2015).
23. H. Zhao, B. Kuyken, S. Clemmen, F. Leo, A. Subramanian, A. Dhakal, P. Helin, S. Severi, E. Brainis, G. Roelkens, and R. Baets, "Visible-to-near-infrared octave spanning supercontinuum generation in a silicon nitride waveguide," Opt. Lett. **40**(10), 2177–2180 (2015).
24. A. R. Johnson, A. S. Mayer, A. Klenner, K. Luke, E. S. Lamb, M. R. Lamont, C. Joshi, Y. Okawachi, F. W. Wise, U. Lipson, M. Keller, and A. L. Gaeta, "Octave-spanning coherent supercontinuum generation in a silicon nitride waveguide," Opt. Lett. **40**(21), 5117–5120 (2015).
25. J. P. Epping, T. Hellwig, M. Hoekman, R. Mateman, A. Leinse, R. G. Heideman, A. van Rees, P. J. van der Slot, C. J. Lee, C. Fallnich, and K.-J. Boller, "On-chip visible-to-infrared supercontinuum generation with more than 495 THz spectral bandwidth," Opt. Express **23**(15), 19596–19604 (2015).
26. M. Montesinos-Ballester, C. Lafforgue, J. Frigerio, A. Ballabio, V. Vakarin, Q. Liu, J. M. Ramirez, X. L. Roux, D. Bouville, A. Barzaghi, C. Alonso-Ramos, L. Vivien, G. Isella, and D. Marris-Morini, "On-chip mid-infrared supercontinuum generation from 3 to 13 μm wavelength," ACS Photonics **7**(12), 3423–3429 (2020).
27. M. Sinobad, C. Monat, B. Luther-Davies, P. Ma, S. Madden, D. J. Moss, A. Mitchell, D. Allioux, R. Orobtchouk, S. Boutami, J.-M. Hartmann, J.-M. Fedeli, and C. Grillet, "Mid-infrared octave spanning supercontinuum generation to 8.5 μm in silicon-germanium waveguides," Optica **5**(4), 360–366 (2018).
28. M. Sinobad, A. DellaTorre, R. Armand, B. Luther-Davies, P. Ma, S. Madden, A. Mitchell, D. J. Moss, J.-M. Hartmann, J.-M. Fedeli, C. Monat, and C. Grillet, "Mid-infrared supercontinuum generation in silicon-germanium all-normal dispersion waveguides," Opt. Lett. **45**(18), 5008–5011 (2020).
29. A. Della Torre, M. Sinobad, R. Armand, B. Luther-Davies, P. Ma, S. Madden, A. Mitchell, D. J. Moss, J.-M. Hartmann, V. Reboud, J.-M. Fedeli, C. Monat, and C. Grillet, "Mid-infrared supercontinuum generation in a low-loss germanium-on-silicon waveguide," APL Photonics **6**(1), 016102 (2021).
30. M. A. Porcel, F. Schepers, J. P. Epping, T. Hellwig, M. Hoekman, R. G. Heideman, P. J. van der Slot, C. J. Lee, R. Schmidt, B. Rudolf, C. Fallnich, and K.-J. Boller, "Two-octave spanning supercontinuum generation in stoichiometric silicon nitride waveguides pumped at telecom wavelengths," Opt. Express **25**(2), 1542–1554 (2017).
31. D. Grassani, E. Tagkoudi, H. Guo, C. Herkommer, F. Yang, T. J. Kippenberg, and C.-S. Brès, "Mid infrared gas spectroscopy using efficient fiber laser driven photonic chip-based supercontinuum," Nat. Commun. **10**(1), 1553 (2019).
32. E. Tagkoudi, D. Grassani, F. Yang, C. Herkommer, T. Kippenberg, and C.-S. Brès, "Parallel gas spectroscopy using mid-infrared supercontinuum from a single Si_3N_4 waveguide," Opt. Lett. **45**(8), 2195–2198 (2020).
33. J. M. Dudley, G. Genty, and S. Coen, "Supercontinuum generation in photonic crystal fiber," Rev. Mod. Phys. **78**(4), 1135–1184 (2006).
34. A. M. Heidt, "Pulse preserving flat-top supercontinuum generation in all-normal dispersion photonic crystal fibers," J. Opt. Soc. Am. B **27**(3), 550–559 (2010).
35. L. Zhang, Y. Yan, Y. Yue, Q. Lin, O. Painter, R. G. Beausoleil, and A. E. Willner, "On-chip two-octave supercontinuum generation by enhancing self-steepening of optical pulses," Opt. Express **19**(12), 11584–11590 (2011).
36. M. Klimczak, G. Soboń, K. Abramski, and R. Buczyński, "Spectral coherence in all-normal dispersion supercontinuum in presence of raman scattering and direct seeding from sub-picosecond pump," Opt. Express **22**(26), 31635–31645 (2014).
37. S. Xing, S. Kharitonov, J. Hu, and C.-S. Brès, "Linearly chirped mid-infrared supercontinuum in all-normal-dispersion chalcogenide photonic crystal fibers," Opt. Express **26**(15), 19627–19636 (2018).
38. T. Le Canh, H. Le Van, D. Pysz, T. B. Dinh, D. T. Nguyen, Q. H. Dinh, M. Klimczak, R. Kasztelanic, J. Pniewski, R. Buczynski, and K. X. Dinh, "Supercontinuum generation in all-normal dispersion suspended core fiber infiltrated with water," Opt. Mater. Express **10**(7), 1733–1748 (2020).
39. S. Christensen, Z. Ye, M. Bache, and V. T. Company, "Octave-spanning frequency comb generation in all-normal-dispersion silicon-rich silicon nitride waveguide," in *CLEO: Science and Innovations*, (Optical Society of America, 2020), p. STu3H.7.
40. M. H. Pfeiffer, J. Liu, A. S. Raja, T. Morais, B. Ghadiani, and T. J. Kippenberg, "Ultra-smooth silicon nitride waveguides based on the damascene reflow process: fabrication and loss origins," Optica **5**(7), 884–892 (2018).
41. J. Liu, A. S. Raja, M. H. Pfeiffer, C. Herkommer, H. Guo, M. Zervas, M. Geiselmann, and T. J. Kippenberg, "Double inverse nanotapers for efficient light coupling to integrated photonic devices," Opt. Lett. **43**(14), 3200–3203 (2018).
42. K. Ikeda, R. E. Saperstein, N. Alic, and Y. Fainman, "Thermal and Kerr nonlinear properties of plasma-deposited silicon nitride/silicon dioxide waveguides," Opt. Express **16**(17), 12987–12994 (2008).
43. A. Rampur, D.-M. Spangenberg, G. Stępniewski, D. Dobrakowski, K. Tarnowski, K. Stefańska, A. Paździor, P. Mergo, T. Martynkien, T. Feurer, and M. Klimczak, "Temporal fine structure of all-normal dispersion fiber supercontinuum pulses caused by non-ideal pump pulse shapes," Opt. Express **28**(11), 16579–16593 (2020).